

## Article

# Synthesis, Characterization and Photocatalytic Activity of Spherulite-like *r*-TiO<sub>2</sub> in Hydrogen Evolution Reaction and Methyl Violet Photodegradation

Anastasia K. Bachina <sup>1,\*</sup>, Vadim I. Popkov <sup>1,\*</sup>, Anna S. Seroglazova <sup>1</sup>, Maria O. Enikeeva <sup>1</sup>, Anna Yu. Kurenkova <sup>2</sup>, Ekaterina A. Kozlova <sup>2</sup>, Evgeny Y. Gerasimov <sup>2</sup>, Albina A. Valeeva <sup>3</sup> and Andrey A. Rempel <sup>4</sup>

<sup>1</sup> Ioffe Institute, Russian Academy of Sciences, 194021 Saint-Petersburg, Russia

<sup>2</sup> Boreskov Institute of Catalysis of the Siberian Branch, Russian Academy of Sciences, 630090 Novosibirsk, Russia

<sup>3</sup> Institute of Solid State Chemistry, Ural Branch of the Russian Academy of Sciences, 620990 Ekaterinburg, Russia

<sup>4</sup> Institute of Metallurgy, Ural Branch of the Russian Academy of Sciences, 620016 Ekaterinburg, Russia

\* Correspondence: a.k.bachina@yandex.ru (A.K.B.); vadim.i.popkov@mail.ioffe.ru (V.I.P.)



**Citation:** Bachina, A.K.; Popkov, V.I.; Seroglazova, A.S.; Enikeeva, M.O.; Kurenkova, A.Y.; Kozlova, E.A.; Gerasimov, E.Y.; Valeeva, A.A.; Rempel, A.A. Synthesis, Characterization and Photocatalytic Activity of Spherulite-like *r*-TiO<sub>2</sub> in Hydrogen Evolution Reaction and Methyl Violet Photodegradation. *Catalysts* **2022**, *12*, 1546. <https://doi.org/10.3390/catal12121546>

Academic Editors: Farid Orudzhev and Irina A. Zvereva

Received: 29 October 2022

Accepted: 27 November 2022

Published: 1 December 2022

**Publisher's Note:** MDPI stays neutral with regard to jurisdictional claims in published maps and institutional affiliations.



**Copyright:** © 2022 by the authors. Licensee MDPI, Basel, Switzerland. This article is an open access article distributed under the terms and conditions of the Creative Commons Attribution (CC BY) license (<https://creativecommons.org/licenses/by/4.0/>).

**Abstract:** Synthesis and characterization of spherulite-like nanocrystalline titania with rutile structure (*r*-TiO<sub>2</sub>) are described herein. The *r*-TiO<sub>2</sub> particles were synthesized via the convenient and low-cost hydrothermal treatment of TiO(C<sub>6</sub>H<sub>6</sub>O<sub>7</sub>) titanyl citrate. The *r*-TiO<sub>2</sub> spherulites are micron-sized agglomerates of rod-shaped nanocrystals with characteristic sizes of 7(±2) × 43(±10) nm, oriented along (101) crystallographic direction, and separated by micropores, as revealed by SEM and TEM. PXRD and Raman spectroscopy confirmed the nanocrystalline nature of *r*-TiO<sub>2</sub> crystallites. BET analysis showed a high specific surface area of 102.6 m<sup>2</sup>/g and a pore volume of 6.22 mm<sup>3</sup>/g. Photocatalytic performances of the *r*-TiO<sub>2</sub> spherulites were investigated for the processes of methyl violet (MV) degradation in water and hydrogen evolution reaction (HER) in aqueous solutions of ethanol. The (MV) degradation kinetics was found to be first-order and the degradation rate coefficient is 2.38 × 10<sup>-2</sup> min<sup>-1</sup>. The HER was performed using pure *r*-TiO<sub>2</sub> spherulites and nanocomposite *r*-TiO<sub>2</sub>/Pt spherulites with platinum deposited on the surface (*r*-TiO<sub>2</sub>/Pt). It was discovered that the *r*-TiO<sub>2</sub>/Pt nanocomposite has a 15-fold higher hydrogen evolution rate than pure *r*-TiO<sub>2</sub>; their rates are 161 and 11 nmol/min, respectively. Thus, the facile synthesis route and the high photocatalytic performances of the obtained nanomaterials make them promising for commercial use in such photocatalytic processes as organic contamination degradation and hydrogen evolution.

**Keywords:** titania; rutile; spherulites; hydrothermal synthesis; photocatalysis; hydrogen evolution reaction; methyl violet degradation

## 1. Introduction

With the development of technology and industry, a tendency toward fossil fuel consumption is steadily observed. Moreover, the world is faced with pollutants caused by toxic and harmful substance emissions, manufacturing waste, and a scarcity of resources for renewable energy [1–3].

Nowadays, to reduce environmental pollution, photocatalysts effective for green chemistry are being sought. The photocatalysts should meet demands to absorb visible light and generate free radicals on their surface under photoexcitation in order to completely decompose toxic substances into neutral ones. Solar energy is an important renewable energy source, for now, that may be easily converted to electrical and chemical energy. Thus, cutting-edge technologies using solar power should be rapidly developed to address energy and environmental challenges. One of the best candidates for these challenges is

titanium dioxide ( $\text{TiO}_2$ ), which has received great attention due to its potential application in various fields [1–10]. The popularity of  $\text{TiO}_2$  is primarily associated with the diversity of the functional properties that are provided by a variety of crystal structures, morphology, and size [11–18].  $\text{TiO}_2$  has a set of unique characteristics that allow it to occupy a special place among transition metal oxides due to its high stability, chemical inertness, corrosion resistance, good biocompatibility, low toxicity, and low cost. The ability of titanium dioxide to generate effective electron–hole pairs under solar irradiation, in particular, broadens its applications as a photocatalyst for water photolysis,  $\text{CO}_2$  conversion, hydrogen production, contaminate decomposition, and other potentially green energy-saving technologies.

In this regard, anatase is the most known and widely used polymorphic modification of titania due to the highest value of the band gap (3.2 eV) compared to the other modifications [4]. Anatase, on the other hand, is known to belong to metastable polymorphic modifications, whereas rutile is the only thermodynamically stable structure modification [19], with a band gap of 3.0 eV for bulk samples [4]. Recently, it has been shown that nano-sized rutile may compete with anatase as a photocatalytic material [20]. In light of this, new approaches to synthesizing nanosized rutile and improving its functional properties have begun to emerge.

In a previous study [21], the facile route to synthesize nanocrystalline rutile with the complicated morphology of agglomerated rod-like rutile nanocrystals in the shape of micron-sized spherulite particles (*r*- $\text{TiO}_2$ ) was proposed. It was shown that the spherulite-like rutile particles possess high electrocatalytic activity, which has motivated the further study of the properties of the spherulite rutile particles. The aim of the present study is the synthesis of an effective photocatalyst for green chemistry, possessing a high specific surface and generating free radicals on its surface under photoexcitation for the complete decomposition of harmful substances into non-toxic ones, and hydrogen evolution reaction. For this purpose, a thorough characterization of the spherulite-like rutile particles was carried out. The photocatalytic activity of the *r*- $\text{TiO}_2$  particles was evaluated for the model reaction of methyl violet (MV) degradation and hydrogen evolution reaction (HER). The nanocomposite photocatalyst based on the spherulite-like rutile particles with platinum deposited on their surface (*r*- $\text{TiO}_2/\text{Pt}$ ) was obtained and tested for photocatalytic activity in the HER.

## 2. Results and Discussion

The PXRD pattern of the sample obtained by hydrothermal treatment of titanyl citrate is shown in Figure 1a. According to the phase analysis, the obtained sample is crystalline  $\text{TiO}_2$  with a rutile structure (*r*- $\text{TiO}_2$ ) (sp.gr.  $P4_2/mnm$ ). The general analysis of the shape of the PXRD pattern showed that there is a distinctive broadening of the peaks, which argues for the nanosized nature of the obtained *r*- $\text{TiO}_2$  crystals. Moreover, as one can see from Figure 1a, there is a varying broadening of peaks corresponding to different crystallographic directions, which may be evidence for the morphology anisotropy of the crystallites. The Scherrer equation was used to calculate the average crystallite size along crystallographic directions, which were conditionally referred to two groups with noticeably different broadening: 1—(110), (211), and (112); 2—(101), (111), and (002), yielding noticeably different average values of  $5 \pm 1$  nm for the first group and  $15 \pm 2$  nm for the second, confirming the nanosized nature of the *r*- $\text{TiO}_2$ . Despite the signs of asymmetric morphology of the *r*- $\text{TiO}_2$  nanocrystals, the effects caused by the texture of the crystals along any certain direction were not found. That may both be due to the disordered arrangement of the *r*- $\text{TiO}_2$  nanocrystals in the studied powder or due to a more complex type of their ordering compared to the texture along one direction. This question was illuminated by the results of the SEM and TEM investigations described below.

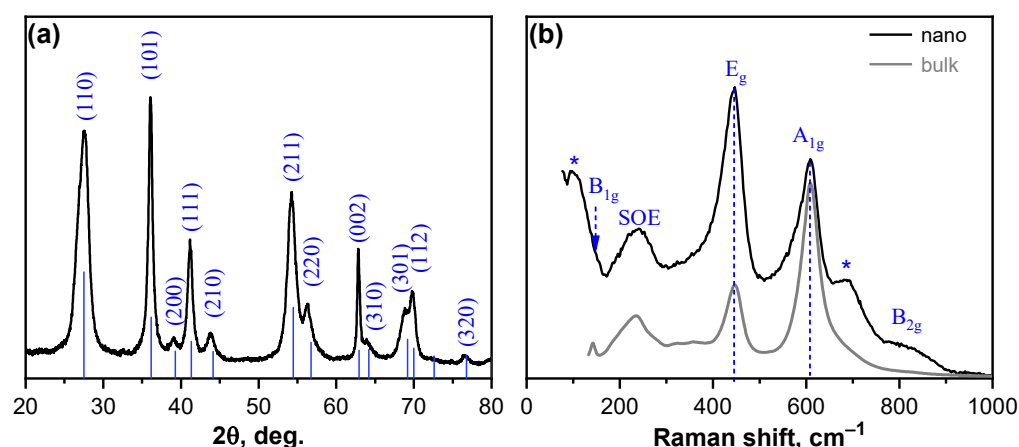


**Figure 1.** PXRD pattern of the rutile  $\text{TiO}_2$  nanocrystals, theoretical XRD pattern of rutile reference from ICSD (# 202241)—(a), Raman spectra of the *r*- $\text{TiO}_2$  nanocrystals synthesized in present work and bulk rutile  $\text{TiO}_2$  from RRUFF database (R110109)—(b). \* Scattering bands found in nanosized rutile.

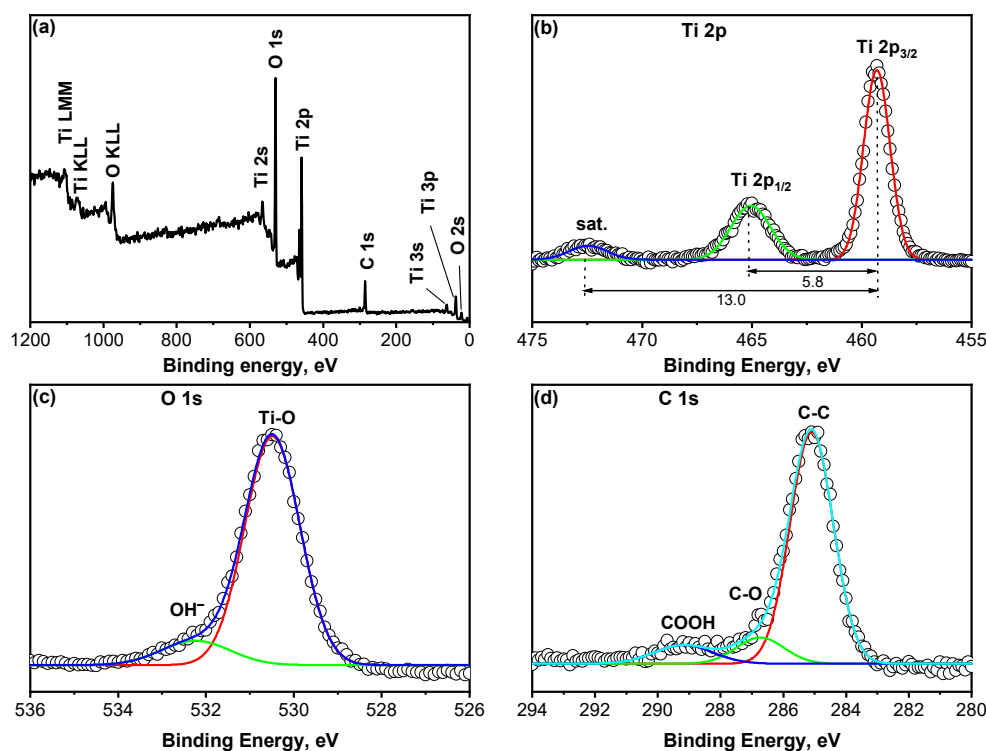
In the Raman spectrum of the rutile nanoparticles shown in Figure 1b one can see six peaks at about 100, 237, 444, 608, 680, and 804  $\text{cm}^{-1}$ . Conventional Raman spectra of bulk rutile are characterized by four first-order modes:  $B_{1g}$  (143),  $E_g$  (447),  $A_{1g}$  (612),  $B_{2g}$  (826), and secondary-order multiply mode (SOE) with a maximum around 230–240  $\text{cm}^{-1}$  [22]. However, it was shown that features of the Raman spectrum of rutile  $\text{TiO}_2$  are size-dependent [23,24]. In particular, such modifications of the Raman spectrum as the appearance of new scattering bands at about 105 and 685  $\text{cm}^{-1}$  (marked with an asterisk in Figure 1b); shifts, asymmetric peak broadening, redistribution of intensities for  $E_g$  and  $A_{1g}$  modes have been detected to be typical for nanocrystalline rutile [25]. In the case of *r*- $\text{TiO}_2$  synthesized here, the following typical features were found: new bands at about 100 and 685  $\text{cm}^{-1}$ , low-frequency peak broadening, changes in intensity maxima for  $E_g$  and  $A_{1g}$  modes, and the impossibility to resolve  $B_{1g}$  mode at about 143  $\text{cm}^{-1}$  due to the appearance of a strong lower frequency band. There is a lack of unanimity in the literature about the origin of additional scattering bands; however, authors agree that they are specific features for Raman spectra of nanocrystalline rutile  $\text{TiO}_2$  [24,26]. Thus, Raman spectroscopy data confirmed that the synthesized sample is rutile, and the specific features of the spectrum correspond to nanosized  $\text{TiO}_2$ .

Figure 2a shows the XPS survey spectrum of the rutile nanoparticles. The photoelectron peak for Ti 2p appears at a binding energy (Eb) of 459.3 eV, O 1s at Eb = 530.5 eV, and C 1s at Eb = 285.1 eV. The OKLL, TiKLL, and TiLMM Auger peaks are at binding energies of 975 eV, 1074 eV, and 1106, respectively [27]. The survey spectrum indicates the presence of Ti, O, and C elements on the surface of the nanoparticles. The carbon probably came from the organic precursor, which was not completely removed from the surface of the nanoparticles, and the adsorbed carbon dioxide.

The high-resolution Ti 2p spectrum of the rutile nanoparticles is shown in Figure 2b. The Ti 2p<sub>3/2</sub> photoelectron line at 459.3 eV, the spin-orbit separation of 5.8 eV, and a satellite peak at 14 eV higher than the main peak are observed and are in good agreement with the reported values [28]. The intensity ratio of Ti 2p<sub>1/2</sub> and Ti 2p<sub>3/2</sub> peaks is about 1:2.

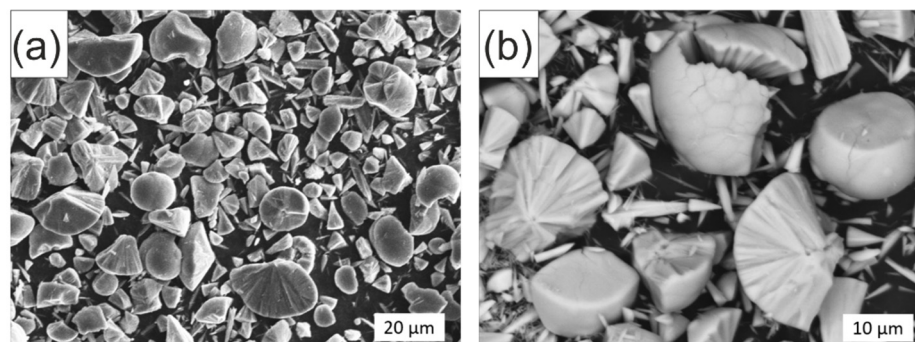
The high-resolution O 1s spectrum shows a main peak at 530.4 eV and a shoulder at 532.3 eV (Figure 2c). The peak at 530.4 eV is attributed to oxygen bound to  $\text{Ti}^{4+}$  in pure oxide and the shoulder is attributed to surface  $\text{OH}^-$  species.

Figure 2d shows the high-resolution XPS spectrum of the C 1s region. There are three peaks at binding energies of 285.1, 286.8, and 289.18 eV, which correspond to C-C, C-O, and COOH bonds [27]. The C element mainly comes from the itaconic acid that is the additive product of  $\text{TiO}_2$  synthesis from the titanyl citrate precursor.



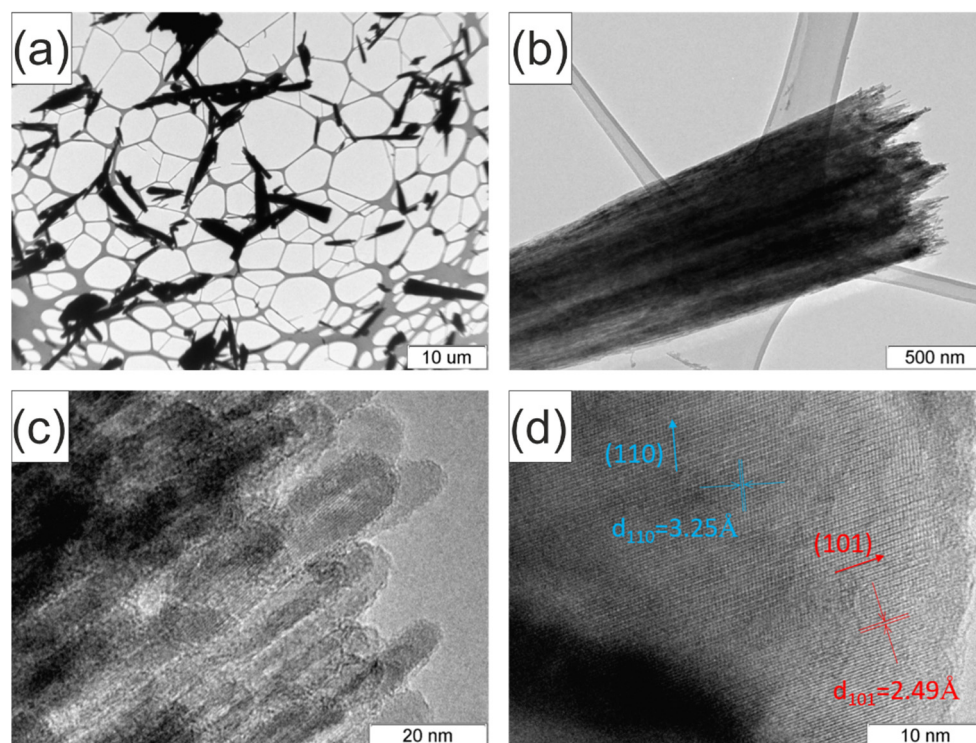
**Figure 2.** XPS spectra of the rutile nanoparticles. (a) XPS survey spectrum; (b–d) are spectra from Ti 2p, O 1s, and C 1s core levels.

Figure 3 shows SEM images of the synthesized *r*-TiO<sub>2</sub>. Analyzing the survey SEM image (Figure 3a) one can see that the *r*-TiO<sub>2</sub> particles have spherulite-like morphology. The size of spherulite-like particles ranges from a few to tens of microns. The more detailed picture (Figure 3b) demonstrates that the spherulite-like formations are mostly segmented and are different parts of spherulite, such as spherical cones and caps. Their shapes vary from almost a whole sphere to a spherical cone close to a needle-like shape. Examining the separate part of spherulite (Figure 3b), one can see that it has a complex structure, which consists of separate elements (*r*-TiO<sub>2</sub> crystals) arranged from a spherulite center to an external surface. Features of *r*-TiO<sub>2</sub> crystal arrangement were studied by TEM.



**Figure 3.** SEM images of rutile TiO<sub>2</sub> spherulites at different magnifications: 20 μm (a), 10 μm (b).

In Figure 4 representative TEM images of the *r*-TiO<sub>2</sub> spherulite cones are shown. According to the data, only small spherulite cones got onto the specimen grid for examination. This is markedly evident when comparing the TEM image in Figure 4a with the SEM image in Figure 2. At higher magnification, the crystal structure of the surface of one of the spherulite cones is revealed, and one can see that it consists of specifically oriented *r*-TiO<sub>2</sub> nanocrystals with rod-like morphology (Figure 4b).



**Figure 4.** TEM images of  $r$ -TiO<sub>2</sub> spherulites at different magnifications at different magnifications: 10  $\mu$ m (a), 500 nm (b), 20 nm (c), 10 nm (d).

Due to the TEM data, the diameter of the rods was estimated to be 5–7 nm. This value coincides with the average size of the crystallite domain along (110) crystallographic direction calculated from PXRD data. The length of the rods was not possible to determine precisely; however, the assessed value of the length can be considered in the range of 20–30 nm, which is comparable with the average size of the crystallite domain along (101) crystallographic direction.

Comparing this data with the results of the SEM investigation, one can conclude that the synthesized spherulites consist of oriented crystals of  $r$ -TiO<sub>2</sub> with rod-like morphology and a length considerably smaller than the spherulite radius. In other words, the spherulite-like particles of titania are agglomerates of oriented crystal  $r$ -TiO<sub>2</sub> nanorods. Analyzing the crystal structure of the individual  $r$ -TiO<sub>2</sub> nano-rod via TEM (Figure 4d) it was established that it is oriented within a spherulite along (101) crystallographic direction, and the smallest size which is the diameter of the nano-rod corresponds to (110) crystallographic direction.

To gain more characteristics about the crystalline structure of the  $r$ -TiO<sub>2</sub> sample, elaborate refinement of the PXRD pattern was conducted. Lattice parameters of  $r$ -TiO<sub>2</sub> refined by the Le Bail method are shown in Figure 5a. Assuming the rod-like morphology of the  $r$ -TiO<sub>2</sub> nanocrystals revealed by TEM analysis, the average 3D morphology was reconstructed from the Le Bail refinement and visualized with VESTA software (insert in Figure 5b). The obtained 3D morphology is in agreement with the TEM data. Using the fundamental parameters model for PXRD pattern refinement, the crystallite size distributions were calculated for the crystallite domains along (110) and (101) crystallographic directions, which correspond to the diameter and length of  $r$ -TiO<sub>2</sub> nanorods (Figure 5b). As can be seen, the shapes of the two distributions are greatly different and confirm the previous findings. Thus, the crystallite distribution plotted in black has a narrow shape and a median size of 6.2 nm, while the other one plotted in red demonstrates a greater spread of values and has a median size of 12.7 nm, which is in good agreement with the average values of the diameter and the length of  $r$ -TiO<sub>2</sub> nanorods (Figure 5b).

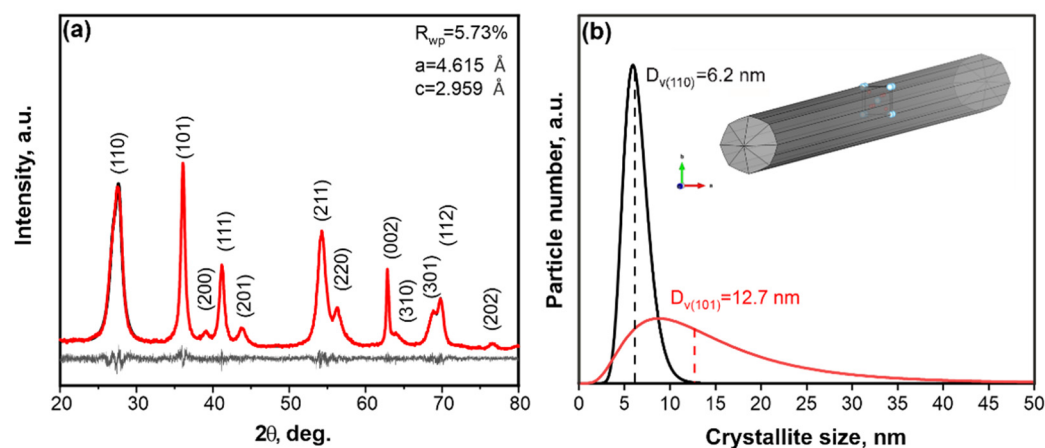


**Figure 5.** (a) Results of the X-ray data refinement in  $P4_2/mnm$  for the  $r$ -TiO<sub>2</sub> sample. (b) Calculated crystallite size distributions for crystallite domains along (110), and (101) crystallographic directions, insert: reconstructed crystallite morphology.

Analysis of the specific surface of the obtained  $r$ -TiO<sub>2</sub> powder and its porosity was carried out by the method of low-temperature nitrogen sorption-desorption. The initial piece of the nitrogen absorption curve was analyzed up to the pressure value  $P/P_0 = 0.25$  (Figure 6a). The value of the specific surface was determined to be  $S = 102.6 \text{ m}^2/\text{g}$  by processing this curve piece using the multipoint BET method and plotting the linear part of the dependence  $1/[Q(P_0/P - 1)] = f(P/P_0)$  (Figure 6a). It is a relatively high value for the specific surface area. That may indicate the presence of pores between individual  $r$ -TiO<sub>2</sub> nanocrystals within a spherulite-like particle, which makes the internal surface of these rod-like nanocrystals accessible for reagents. In addition, the value of constant  $C = 343.7$  in the BET equation is significantly higher than the threshold value of 200, which characterizes the effect on non-porous solids. Thus, it was found that the powder based on spherulites of  $r$ -TiO<sub>2</sub> nanocrystals has a developed porous structure.

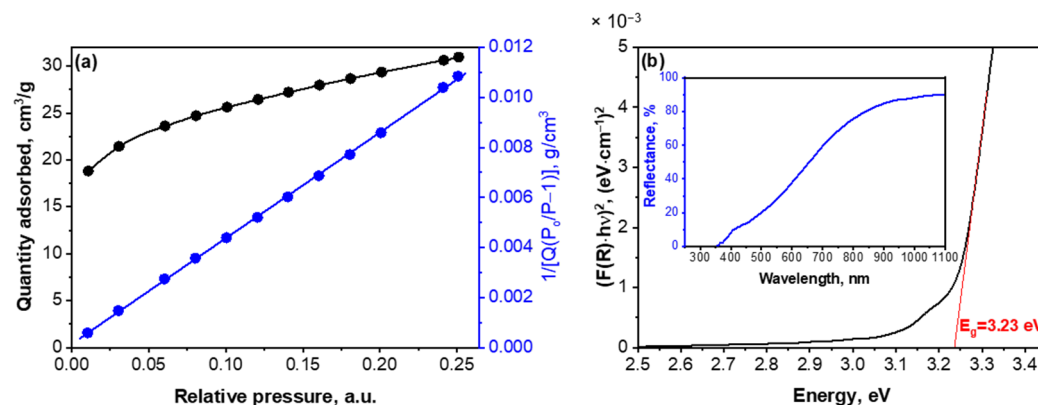


**Figure 6.** (a) Low-temperature nitrogen adsorption isotherms of the  $r$ -TiO<sub>2</sub> spherulites. (b) Tauc plot, insert: diffuse reflectance spectrum.

Analysis of the porous structure of the powder via the t-plot method allowed us to determine the value of the volume of micropores, located in the intercrystalline space of the  $r$ -TiO<sub>2</sub>, of  $6.22 \text{ mm}^3/\text{g}$ .  $S_{\text{micro}} = 13.0 \text{ m}^2/\text{g}$ , or 12.7%, of the total specific surface area, is contributed by this micropore area. The external surface area accounts for  $89.6 \text{ m}^2/\text{g}$ , or 87.3%. Thus, the pores between the  $r$ -TiO<sub>2</sub> nanocrystals determine the microporous structure of the synthesized spherulites and have a significant effect on their surface.

To determine the band gap of the  $r$ -TiO<sub>2</sub> sample, UV DRS was used. The diffuse reflectance spectrum is shown in Figure 6b. The data obtained showed that the  $r$ -TiO<sub>2</sub> spherulites actively absorb light beginning around 400 nm and below; the absorption edge

is 384 nm. The optical absorption edge has an almost linear shape and does not have noticeable inflections or overlaps, which is associated with the high chemical and phase purity of the *r*-TiO<sub>2</sub> nanocrystals and their morphological homogeneity.

Using the Kubelka–Munk function, the diffuse reflectance spectrum was converted to an absorbance mode [29]. Based on the assumption of allowed direct transitions, the optical band gap was defined using the Tauc method [30]. The band gap value is 3.23 eV. The perception that the different terminal facets may have different values for the band gaps was confirmed by computations and measurements. Most profoundly, it was completed for anatase faceted crystals; the rutile ones are much less studied [31–34]. In addition to that, as *r*-TiO<sub>2</sub> nanocrystals have a size of less than 10 nm in one of the dimensions, the quantum size effect cannot be excluded. The influence of size and shape on the band gap of different nanoscale semiconductors has been shown in the literature [35–37]. Thus, the unusually wide band gap of the synthesized rutile nanocrystals, whose value is more characteristic for titanium dioxide with the anatase structure (*a*-TiO<sub>2</sub>), is apparently related to the morphological peculiarities of the *r*-TiO<sub>2</sub> nanocrystals, which have an anisotropic shape along the (101) crystallographic direction.

The photocatalytic activity of *r*-TiO<sub>2</sub> spherulites was evaluated via the conventional methyl violet (MV) degradation under UV light irradiation. With irradiation time increasing, one can see that MV degradation increased as depicted by the Vis absorbance spectra (Figure 7a). The decomposition of MV dye can be affected by direct photolysis and photocatalysis with photolysis. To evaluate the contributions of both effects and assess the effect of solely *r*-TiO<sub>2</sub>, the kinetic dependencies of MV concentration were calculated and linearized in accordance with the model of the pseudo-first reaction order via logarithmic transformation (Figure 7b). As can be seen, direct photolysis has a minor effect on MV decomposition, as only 40% of MV is degraded after 90 min of UV light irradiation, whereas MV degradation reaches 90% after the same time in the presence of *r*-TiO<sub>2</sub> spherulites. Thus, *r*-TiO<sub>2</sub> spherulites demonstrate considerable photocatalytic activity due to their surficial and structural properties described above (Table 1). The rate constants estimated for photolysis, photocatalysis, and photocatalysis plus photolysis are shown in Figure 7c.

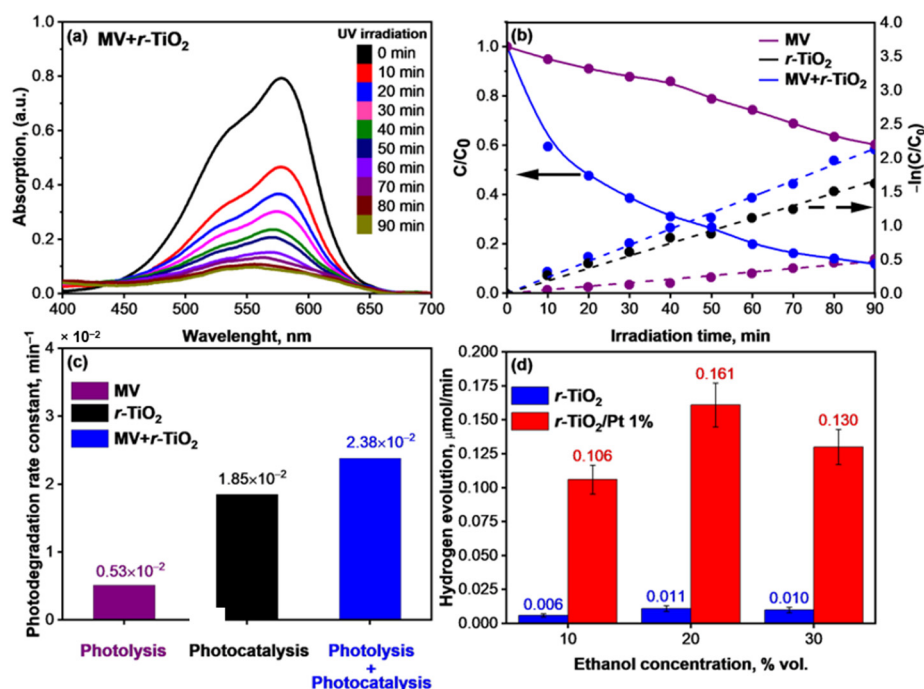


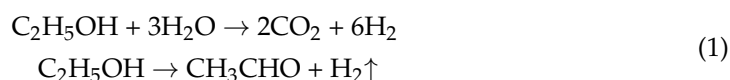
**Figure 7.** (a) Photodegradation of methyl violet aqueous solution in the presence of *r*-TiO<sub>2</sub> spherulites. (b) Normalized and logarithmic kinetics curves of MV photodegradation in the presence and absence of *r*-TiO<sub>2</sub> spherulites. (c,d) Hydrogen evolution rates for aqueous solutions of ethanol with concentrations of 10, 20, and 30 vol% in the presence of *r*-TiO<sub>2</sub> spherulites and *r*-TiO<sub>2</sub>/Pt nanocomposite.

**Table 1.** Structural characteristics of different photocatalysts, their synthesis background, and photocatalytic properties.

Sample	Phase Composition	$S_s$ , $m^2/g$	Morphology/ Crystallite Size, nm	Synthesis Procedure/ Precursor	$k$ , $min^{-1}$	Reference
<i>r</i> -TiO <sub>2</sub>	Rutile	102.6	Spherulite agglomerates of rod-like/5 × 15	HTT */ titanyl citrate	0.0238	this work
TiO <sub>2</sub>	Brookite	93.4	Sponge-like/30	HTT */ titanium (IV) peroxocomplex	0.0234	[12]
TNS	Anatase, rutile	207	Sheet-like	HTT *, Degussa P25	0.01812	[38]
TiO <sub>2</sub>	Anatase	~36	12.3	Sol-gel, titanium(IV) butoxide	0.00994	[39]
TiO <sub>2</sub>	Anatase	106.1	8.7	Sol-gel, titanium(IV) butoxide, activated carbone	0.03914	[7]
TiO <sub>2</sub>	Rutile	-	Agglomerated flakes/53	Sol-gel/ TiCl <sub>4</sub>	0.01156	[40]
FRT	Rutile	-	Agglomerated flakes/39	Impregnation TiO <sub>2</sub> with HF	0.02541	[40]
SRT	Rutile, silver	-	Agglomerated flakes/48	Photoreduction of AgNO <sub>3</sub> on TiO <sub>2</sub>	0.02827	[40]

\*—Hydrothermal treatment.

The evolution of hydrogen from aqueous–alcoholic solutions at exposure to UV radiation in the presence of a photocatalyst is a model process used to evaluate and compare the activity of substances of different compositions and structures. In this work, the photocatalytic activity of spherulites based on *r*-TiO<sub>2</sub> was measured in the process of hydrogen evolution from an aqueous solution of ethanol with concentrations of 10, 20, and 30 vol% under UV radiation with the wavelength of 380 nm. The general chemical equation describing the whole process and the reaction equation describing the first stage of the process can be represented as follows [41]:



In Figure 7d, the results of photocatalytic tests for samples of spherulites based on *r*-TiO<sub>2</sub> before and after 1 wt% platinum (Pt) deposition are shown. According to the data, initial *r*-TiO<sub>2</sub> nanocrystals do not reveal noticeable photocatalytic activity, regardless of the concentration of ethanol in the solution, and the hydrogen evolution rate does not exceed 11 nmol/min. However, after Pt deposition on the surface of the *r*-TiO<sub>2</sub> spherulites, the photocatalytic activity drastically increases, and the maximum released amount of hydrogen is 161 nmol/min, which is almost 15 times higher than for platinum-free spherulites. The addition of platinum causes a significant change in the photocatalytic activity of *r*-TiO<sub>2</sub> nanocrystals, which is associated with an increase in charge separation efficiency and, as a result, a decrease in electron–hole pair recombination processes [42].

The dependence on the ethanol concentration provides another important piece of information about the activity of spherulites based on *r*-TiO<sub>2</sub> (Figure 7d). As a rule, the concentration of ethanol in biomass processing products does not exceed 30 vol% [43,44]. Therefore, the study of photocatalytic activity was carried out in aqueous solutions of ethanol with concentrations of 10, 20, and 30 vol%. The dependence of the hydrogen evolution rate on the concentration of ethanol has a maximum concentration value of 20 vol%, which is observed both for the initial spherulites based on *r*-TiO<sub>2</sub>, and for

spherulites with platinum. The maximum hydrogen evolution rate is 161 nmol/min, or in other words, 193  $\mu\text{mol}$  of hydrogen per gram of photocatalyst per hour. The presence of an extremum in the concentration dependence can indicate the governing influence of ethanol sorption processes and desorption processes of the intermediate reaction product, acetaldehyde, on the photocatalyst surface. At low ethanol concentrations (10 vol%), the process of photocatalytic hydrogen evolution is apparently limited by the rate of ethanol diffusion on the surface of spherulites based on *r*-TiO<sub>2</sub>. In the case of high ethanol concentrations (30 vol%), the rate of the entire process is limited by the removal of the product of photocatalytic interaction, liquid acetaldehyde, which is hindered by the excess of ethanol in the solution. At an ethanol concentration of 20 vol%, there is observed some semblance of an optimum equilibrium between the rates of sorption of the reagent (ethanol), desorption of the product (acetaldehyde), and the photocatalytic reaction, simultaneously occurring on the surface of *r*-TiO<sub>2</sub> spherulites.

### 3. Materials and Methods

#### 3.1. Synthesis Procedure

To obtain *r*-TiO<sub>2</sub> catalyst, titanyl citrate TiO(C<sub>6</sub>H<sub>6</sub>O<sub>7</sub>) was dissolved in distilled water to form a 5 mM reaction solution. Additional ultrasonic treatment for 15 min was used to obtain a stable suspension of titanyl citrate. The suspension was hydrothermally treated in a stainless steel autoclave with a Teflon liner at 225 °C and 3 MPa within 4 h. The precipitate obtained was washed 5 times with distilled water. After drying at 70 °C until complete evaporation of the solvent, a white disperse powder was analyzed.

The *r*-TiO<sub>2</sub>/Pt catalyst was prepared by the method [45,46] of the *r*-TiO<sub>2</sub> powder impregnation in an aqueous solution of H<sub>2</sub>PtCl<sub>6</sub> hexachloroplatinic acid followed by treatment with an aqueous solution of NaBH<sub>4</sub> sodium borohydride. The following chemical reaction occurred, during which the metallic Pt was deposited on the surface of the *r*-TiO<sub>2</sub> particles:



As a result, as previously demonstrated in [47], platinum is deposited on the TiO<sub>2</sub> surface in the form of well-crystallized metallic nanoparticles distributed uniformly across the surface. Thus, the *r*-TiO<sub>2</sub>/Pt nanocomposite obtained by the same procedure in this work is assumed to have the same nature of platinum particle distribution on the surface.

#### 3.2. Physico-Chemical Characterization

Powder X-ray diffraction (PXRD) patterns were recorded using a diffractometer Rigaku SmartLab 3 (Tokyo, Japan) with Cu K $\alpha$  radiation ( $\lambda = 154.056$  pm). The average crystallite size was determined using the SmartLab Studio IV software package from Rigaku. The structure was refined using the decomposition method (Le Bail) [48]. The calculation of the crystallite size distribution was carried out using the method of fundamental parameters in lognormal distribution approximation. The reconstruction of the model of crystallite of *r*-TiO<sub>2</sub> was performed in VESTA [49]. The Raman spectra were obtained with a dispersive confocal Raman spectrometer (Senterra Bruker Optik GmbH, Ettlingen, Germany). A continuous laser beam was focused down to a  $\mu\text{m}$  size spot (spatial resolution) on the sample through a microscope (Olympus BX51, Tokyo, Japan objective 50 $\times$ ) with an excitation of 785 nm (laser power 100 mW). The confocal instrument set-up was set to 50  $\times$  1000  $\mu\text{m}$  and the spectral resolution is 2  $\text{cm}^{-1}$ . XPS spectra were obtained on an «ESCALAB 250Xi» X-ray spectrometer (Thermo Fisher Scientific, Waltham, MA, USA) with Al K $\alpha$  radiation. Scanning electron microscopy (SEM) investigation was performed on a Carl Zeiss EVO 40 (Oberkochen, Germany) using a secondary electron detector. Transmission electron microscopy (TEM) investigation was performed on JEM-2010 (JEOL, Tokyo, Japan) with an accelerating voltage of 200 kV. The Brunauer–Emmett–Teller (BET) surface area was determined by nitrogen adsorption isotherm measurements at 77 K on a Micromeritics ASAP 2020 nitrogen adsorption apparatus (Unterschleißheim, Germany). Micropore vol-

ume and specific surface area of the sample were calculated by the t-plot approach using adsorption isotherm data. Diffuse reflectance spectroscopy (DRS) was performed on a spectrophotometer Specord 200 equipped with an integrating sphere. The spectrum was obtained relative to an optical reference (MgO) in the wavelength range from 350 to 420 nm. The band gap was determined from the position of the edge of the absorption band of the spectrum according to the method described in the work [30].

### 3.3. Photocatalytic Experiments

The photocatalytic methyl violet (MV) degradation was studied in aqueous solutions of pure MV and in the presence of the *r*-TiO<sub>2</sub> catalyst under a UV radiation source—an ozone lamp with a power of 20 W and a wavelength of  $\lambda \leq 400$  nm. The volume of the studying solution was 25 mL, and the concentrations of the catalyst and dye were 0.5 g/L and 0.0232 g/L, respectively. The solutions were placed in an experimental setup, which was an insulated box with a magnetic stirrer and a UV radiation source. Before starting the photocatalytic experiment, the solutions were kept in the dark for 20 min with continuous stirring to establish adsorption equilibrium. After this time, the solutions were irradiated with UV light with a sampling of 5 mL every 10 min to determine the change in the concentration of the dye and plot kinetic curves. The dye concentration was measured using an AvaSphere-30-Refl spectrometer (Apeldoorn, Netherlands) with an AvaLight-XE light source. The total exposure time was 90 min.

The photocatalytic hydrogen evolution was studied in aqueous solutions of ethanol with concentrations of 10, 20, and 30 vol%. Deionized water and sodium hydroxide (with a concentration of 0.1 mol/L) were used for solution preparation. As the photocatalysts, initial *r*-TiO<sub>2</sub> spherulites and *r*-TiO<sub>2</sub> spherulites with deposited platinum (*r*-TiO<sub>2</sub>/Pt) were used in the amount of 0.5 g/L. The temperature of 25 °C was maintained during the 120 min experiment. A LED lamp with an emission maximum of 380 nm was employed as an excitation source. Platinum was deposited from an aqueous solution of H<sub>2</sub>PtCl<sub>6</sub> on the surface of the *r*-TiO<sub>2</sub> according to the procedure described in detail elsewhere [50]. The calculated metal loading was 1 wt%.

## 4. Conclusions

In this work, the synthesis of spherulites based on titanium dioxide nanocrystals by the facile hydrothermal treatment of titanyl citrate was carried out. It was found that the nanocrystals have a rutile structure and are rod-like crystal nanoparticles with an average diameter and length of 5 and 15 nm, respectively. These nanocrystals form micron spherical aggregates in which they are oriented from a common center to the surface of the sphere, thereby forming spherulite-like structures. It is shown that there are pores between crystallites in spherulites, and the resulting substance has a highly developed surface area of 102.6 m<sup>2</sup>/g. The band gap of spherulites based on *r*-TiO<sub>2</sub> is 3.20 eV, which determines their photocatalytic activity under ultraviolet radiation. The photocatalytic activity of the *r*-TiO<sub>2</sub> spherulites in the MV degradation reaction, characterized by the rate constant of  $2.38 \times 10^{-2} \text{ min}^{-1}$ , is decent and, according to the literature, is equal to or even higher than one of the other TiO<sub>2</sub> photocatalysts. The photocatalytic activity of the obtained spherulites, studied in the reaction of hydrogen evolution from ethanol, increases when metallic platinum is deposited on their surface, which is due to an increase in the efficiency of charge separation. An analysis of the concentration dependence of the hydrogen evolution rate indicates the presence of kinetic difficulties in the sorption of ethanol and the desorption of acetaldehyde in the considered photocatalytic process. Based on these results, an ethanol concentration of 20 vol% can be recommended as optimal for photocatalytic hydrogen evolution from an aqueous ethanol solution in the presence of spherulites based on *r*-TiO<sub>2</sub>/Pt. The rate of hydrogen evolution, in this case, is maximum and amounts to 161 nmol/min.

**Author Contributions:** Conceptualization, A.A.R., A.A.V. and V.I.P.; investigation, A.K.B., A.S.S., M.O.E., A.Y.K., E.A.K. and E.Y.G.; writing—original draft preparation, V.I.P. and A.K.B.; writing—review and editing, A.A.V. and E.A.K.; visualization, A.K.B. and M.O.E.; supervision, A.A.R. All authors have read and agreed to the published version of the manuscript.

**Funding:** This research received no external funding.

**Data Availability Statement:** Not applicable.

**Acknowledgments:** The authors are grateful to the PMSI Research Center of SPbSU, Russia for the help in XPS and Raman studies. The powder XRD study was performed on the equipment of the Engineering Center of the Saint Petersburg State Institute of Technology. SEM was performed on the equipment of the Center of Collective Use «Ural M» of the IMET UB RAS. This work was carried out in accordance with the state assignment of the ISSC UB RAS (# 0397-2019-0001) and Ioffe Institute (# 0034-2019-0002). The authors are grateful to Natalia V. Zakharova from SPbSTU, Russia for the DRS study.

**Conflicts of Interest:** The authors declare no conflict of interest.

## References

1. Zhang, X.; Cui, H.; Humayun, M.; Qu, Y.; Fan, N.; Sun, X.; Jing, L. Exceptional Performance of Photoelectrochemical Water Oxidation of Single-Crystal Rutile TiO<sub>2</sub> Nanorods Dependent on the Hole Trapping of Modified Chloride. *Sci. Rep.* **2016**, *6*, 21430. [[CrossRef](#)] [[PubMed](#)]
2. Humayun, M.; Raziq, F.; Khan, A.; Luo, W. Modification Strategies of TiO<sub>2</sub> for Potential Applications in Photocatalysis: A Critical Review. *Green Chem. Lett. Rev.* **2018**, *11*, 86–102. [[CrossRef](#)]
3. Guo, Q.; Zhou, C.; Ma, Z.; Yang, X. Fundamentals of TiO<sub>2</sub> Photocatalysis: Concepts, Mechanisms, and Challenges. *Adv. Mater.* **2019**, *31*, 1901997. [[CrossRef](#)] [[PubMed](#)]
4. Hanaor, D.A.H.; Sorrell, C.C. Review of the Anatase to Rutile Phase Transformation. *J. Mater. Sci.* **2011**, *46*, 855–874. [[CrossRef](#)]
5. Dagherir, R.; Drogui, P.; Robert, D. Modified TiO<sub>2</sub> for Environmental Photocatalytic Applications: A Review. *Ind. Eng. Chem. Res.* **2013**, *52*, 3581–3599. [[CrossRef](#)]
6. Selishchev, D.; Stepanov, G.; Sergeeva, M.; Solovyeva, M.; Zhuravlev, E.; Komissarov, A.; Richter, V.; Kozlov, D. Inactivation and Degradation of Influenza A Virus on the Surface of Photoactive Self-Cleaning Cotton Fabric Functionalized with Nanocrystalline TiO<sub>2</sub>. *Catalysts* **2022**, *12*, 1298. [[CrossRef](#)]
7. Xu, M.; Gao, Y.; Moreno, E.M.; Kunst, M.; Muhler, M.; Wang, Y.; Idriss, H.; Wöll, C. Photocatalytic Activity of Bulk TiO<sub>2</sub> Anatase and Rutile Single Crystals Using Infrared Absorption Spectroscopy. *Phys. Rev. Lett.* **2011**, *106*, 138302. [[CrossRef](#)]
8. Rempel, A.A.; Valeeva, A.A. Nanostructured Titanium Dioxide for Medicinal Chemistry. *Russ. Chem. Bull.* **2019**, *68*, 2163–2171. [[CrossRef](#)]
9. Rempel, A.A.; Kuznetsova, Y.V.; Dorosheva, I.B.; Valeeva, A.A.; Weinstein, I.A.; Kozlova, E.A.; Saraev, A.A.; Selishchev, D.S. High Photocatalytic Activity Under Visible Light of Sandwich Structures Based on Anodic TiO<sub>2</sub>/CdS Nanoparticles/Sol-Gel TiO<sub>2</sub>. *Top. Catal.* **2020**, *63*, 130–138. [[CrossRef](#)]
10. Rempel, A.A.; Valeeva, A.A.; Vokhmintsev, A.S.; Weinstein, I.A. Titanium Dioxide Nanotubes: Synthesis, Structure, Properties and Applications. *Russ. Chem. Rev.* **2021**, *90*, 1397–1414. [[CrossRef](#)]
11. Swamy, V.; Gale, J.D.; Dubrovinsky, L.S. Atomistic Simulation of the Crystal Structures and Bulk Moduli of TiO<sub>2</sub> Polymorphs. *J. Phys. Chem. Solids* **2001**, *62*, 887–895. [[CrossRef](#)]
12. Gurenko, V.E.; Popkov, V.I. Hydrothermal-Assisted Synthesis of Sponge-like Brookite for Pseudo-Fenton Decomposition of Crystal Violet under UV-Light. *Nano-Struct. Nano-Objects* **2021**, *28*, 100801. [[CrossRef](#)]
13. Bachina; Almjashaeva, O.V.; Popkov, V.I.; Nevedomskiy, V.N.; Gusarov, V.V. Heat-Stimulated Crystallization and Phase Transformation of Titania Nanoparticles. *J. Cryst. Growth* **2021**, *576*, 126371. [[CrossRef](#)]
14. Kumar, S.; Verma, N.K.; Singla, M.L. Size Dependent Reflective Properties of TiO<sub>2</sub> Nanoparticles and Reflectors Made Thereof. *Dig. J. Nanomater. Biostruct.* **2012**, *7*, 607–619.
15. Huber, B.; Brodyanski, A.; Scheib, M.; Orendorz, A.; Ziegler, C.; Gnaser, H. Nanocrystalline Anatase TiO<sub>2</sub> Thin Films: Preparation and Crystallite Size-Dependent Properties. *Thin Solid Films* **2005**, *472*, 114–124. [[CrossRef](#)]
16. Vasilevskaia, A.K.; Popkov, V.I.; Valeeva, A.A.; Rempel, A.A. Formation of Nonstoichiometric Titanium Oxides Nanoparticles Ti<sub>n</sub>O<sub>2n-1</sub> upon Heat-Treatments of Titanium Hydroxide and Anatase Nanoparticles in a Hydrogen Flow. *Russ. J. Appl. Chem.* **2016**, *89*, 1211–1220. [[CrossRef](#)]
17. Dorosheva, I.B.; Valeeva, A.A.; Rempel, A.A.; Trestsova, M.A.; Utepova, I.A.; Chupakhin, O.N. Synthesis and Physicochemical Properties of Nanostructured TiO<sub>2</sub> with Enhanced Photocatalytic Activity. *Inorg. Mater.* **2021**, *57*, 503–510. [[CrossRef](#)]
18. Valeeva, A.A.; Dorosheva, I.B.; Kozlova, E.A.; Sushnikova, A.A.; Kurenkova, A.Y.; Saraev, A.; Schroettner, H.; Rempel, A. Solar Photocatalysts Based on Titanium Dioxide Nanotubes for Hydrogen Evolution from Aqueous Solutions of Ethanol. *Int. J. Hydrogen Energy* **2021**, *46*, 16917–16924. [[CrossRef](#)]

19. Barnard, A.S.; Zapol, P. Predicting the Energetics, Phase Stability, and Morphology Evolution of Faceted and Spherical Anatase Nanocrystals. *J. Phys. Chem. B* **2004**, *108*, 18435–18440. [[CrossRef](#)]
20. Li, Y.; Lee, N.H.; Lee, E.G.; Song, J.S.; Kim, S.J. The Characterization and Photocatalytic Properties of Mesoporous Rutile TiO<sub>2</sub> Powder Synthesized through Self-Assembly of Nano Crystals. *Chem. Phys. Lett.* **2004**, *389*, 124–128. [[CrossRef](#)]
21. Popkov, V.I.; Bachina, A.K.; Valeeva, A.A.; Lobinsky, A.A.; Gerasimov, E.Y.; Rempel, A.A. Synthesis, Morphology and Electrochemical Properties of Spherulite Titania Nanocrystals. *Ceram. Int.* **2020**, *46*, 24483–24487. [[CrossRef](#)]
22. Zhang, Y.; Harris, C.X.; Wallenmeyer, P.; Murowchick, J.; Chen, X. Asymmetric Lattice Vibrational Characteristics of Rutile TiO<sub>2</sub> as Revealed by Laser Power Dependent Raman Spectroscopy. *J. Phys. Chem. C* **2013**, *117*, 24015–24022. [[CrossRef](#)]
23. Ocaña, M.; Fornés, V.; Ramos, J.V.G.; Serna, C.J. Factors Affecting the Infrared and Raman Spectra of Rutile Powders. *J. Solid State Chem.* **1988**, *75*, 364–372. [[CrossRef](#)]
24. Swamy, V. Size-Dependent Modifications of the First-Order Raman Spectra of Nanostructured Rutile TiO<sub>2</sub>. *Phys. Rev. B-Condens. Matter Mater. Phys.* **2008**, *77*, 15–18. [[CrossRef](#)]
25. Swamy, V.; Muddle, B.C.; Dai, Q. Size-Dependent Modifications of the Raman Spectrum of Rutile TiO<sub>2</sub>. *Appl. Phys. Lett.* **2006**, *89*, 163118. [[CrossRef](#)]
26. Mazza, T.; Barborini, E.; Piseri, P.; Milani, P.; Cattaneo, D.; Li Bassi, A.; Bottani, C.E.; Ducati, C. Raman Spectroscopy Characterization of TiO<sub>2</sub> Rutile Nanocrystals. *Phys. Rev. B-Condens. Matter Mater. Phys.* **2007**, *75*, 045416. [[CrossRef](#)]
27. Moulder, J.F.; Strickle, W.F.; Sobol, P.E.; Bomben, K.D. *Handbook of X-ray Photoelectron Spectroscopy*; Chastain, J., Ed.; Perkin-Elmer Corporation: Eden Prairie, MN, USA, 1995; ISBN 0962702625.
28. Stefanov, P.; Shipochka, M.; Stefchev, P.; Raicheva, Z.; Lazarova, V.; Spassov, L. XPS Characterization of TiO<sub>2</sub> Layers Deposited on Quartz Plates. *J. Phys. Conf. Ser.* **2008**, *100*, 012039. [[CrossRef](#)]
29. Kubelka, P.; Munk, F. Ein Beitrag Zur Optik Der Farbanstriche. *Z. Tech. Phys.* **1931**, *12*, 593–601.
30. Tauc, J.; Grigorovici, R.; Vancu, A. Optical Properties and Electronic Structure of Amorphous Germanium. *Phys. Status Solidi* **1966**, *15*, 627–637. [[CrossRef](#)]
31. Harb, M.; Jeantelot, G.; Basset, J.M. Insights into the Most Suitable TiO<sub>2</sub> Surfaces for Photocatalytic O<sub>2</sub> and H<sub>2</sub> Evolution Reactions from DFT Calculations. *J. Phys. Chem. C* **2019**, *123*, 28210–28218. [[CrossRef](#)]
32. Pan, J.; Liu, G.; Lu, G.Q.; Cheng, H.M. On the True Photoreactivity Order of {001}, {010}, and {101} Facets of Anatase TiO<sub>2</sub> Crystals. *Angew. Chem.-Int. Ed.* **2011**, *50*, 2133–2137. [[CrossRef](#)] [[PubMed](#)]
33. Ruso, J.M.; Verdinelli, V.; Hassan, N.; Pieroni, O.; Messina, P.V. Enhancing CaP Biomimetic Growth on TiO<sub>2</sub> Cuboids Nanoparticles via Highly Reactive Facets. *Langmuir* **2013**, *29*, 2350–2358. [[CrossRef](#)] [[PubMed](#)]
34. Batzill, M. Fundamental Aspects of Surface Engineering of Transition Metal Oxide Photocatalysts. *Energy Environ. Sci.* **2011**, *4*, 3275–3286. [[CrossRef](#)]
35. Viswanatha, R.; Sapra, S.; Satpati, B.; Satyam, P.V.; Dev, B.N.; Sarma, D.D. Understanding the Quantum Size Effects in ZnO Nanocrystals. *J. Mater. Chem.* **2004**, *14*, 661–668. [[CrossRef](#)]
36. Lee, Y.C.; Chang, Y.S.; Teoh, L.G.; Huang, Y.L.; Shen, Y.C. The Effects of the Nanostructure of Mesoporous TiO<sub>2</sub> on Optical Band Gap Energy. *J. Sol-Gel Sci. Technol.* **2010**, *56*, 33–38. [[CrossRef](#)]
37. Singh, M.; Goyal, M.; Devlal, K. Size and Shape Effects on the Band Gap of Semiconductor Compound Nanomaterials. *J. Taibah Univ. Sci.* **2018**, *12*, 470–475. [[CrossRef](#)]
38. Chen, F.; Fang, P.; Gao, Y.; Liu, Z.; Liu, Y.; Dai, Y. Effective Removal of High-Chroma Crystal Violet over TiO<sub>2</sub>-Based Nanosheet by Adsorption-Photocatalytic Degradation. *Chem. Eng. J.* **2012**, *204–205*, 107–113. [[CrossRef](#)]
39. Gao, Z.; Wu, Z.; Chen, X.; Yang, X. Effective Synthesis of Nanoscale Anatase TiO<sub>2</sub> Single Crystals Using Activated Carbon Template to Enhance the Photodegradation of Crystal Violet. *Appl. Organomet. Chem.* **2019**, *33*, e4664. [[CrossRef](#)]
40. Devi, L.G.; Nithya, P.M.; Abraham, C.; Kavitha, R. Influence of Surface Metallic Silver Deposit and Surface Fluorination on the Photocatalytic Activity of Rutile TiO<sub>2</sub> for the Degradation of Crystal Violet a Cationic Dye under UV Light Irradiation. *Mater. Today Commun.* **2017**, *10*, 1–13. [[CrossRef](#)]
41. Markovskaya, D.V.; Kozlova, E.A. Formal Kinetic Description of Photocatalytic Hydrogen Evolution from Ethanol Aqueous Solutions in the Presence of Sodium Hydroxide. *Kinet. Catal.* **2018**, *59*, 727–734. [[CrossRef](#)]
42. Sun, B.; Vorontsov, A.V.; Smirniotis, P.G. Role of Platinum Deposited on TiO<sub>2</sub> in Phenol Photocatalytic Oxidation. *Langmuir* **2003**, *19*, 3151–3156. [[CrossRef](#)]
43. Moiseev, I.I. Green Chemistry: Development Trajectory. *Russ. Chem. Rev.* **2013**, *82*, 616–623. [[CrossRef](#)]
44. Rodionova, M.V.; Poudyal, R.S.; Tiwari, I.; Voloshin, R.A.; Zharmukhamedov, S.K.; Nam, H.G.; Zayadan, B.K.; Bruce, B.D.; Hou, H.J.M.; Allakhverdiev, S.I. Biofuel Production: Challenges and Opportunities. *Int. J. Hydrogen Energy* **2017**, *42*, 8450–8461. [[CrossRef](#)]
45. Kozlova, E.A.; Markovskaya, D.V.; Cherepanova, S.V.; Saraev, A.A.; Gerasimov, E.Y.; Perevalov, T.V.; Kaichev, V.V.; Parmon, V.N. Novel Photocatalysts Based on Cd<sub>1-x</sub>Zn<sub>x</sub>S/Zn(OH)<sub>2</sub> for the Hydrogen Evolution from Water Solutions of Ethanol. *Int. J. Hydrogen Energy* **2014**, *39*, 18758–18769. [[CrossRef](#)]
46. Kozlova, E.A.; Cherepanova, S.V.; Markovskaya, D.V.; Saraev, A.A.; Gerasimov, E.Y.; Parmon, V.N. Novel Photocatalysts Pt/Cd<sub>1-x</sub>Zn<sub>x</sub>S/ZnO/Zn(OH)<sub>2</sub>: Activation during Hydrogen Evolution from Aqueous Solutions of Ethanol under Visible Light. *Appl. Catal. B Environ.* **2016**, *183*, 197–205. [[CrossRef](#)]

47. Kozlova, E.A.; Kurenkova, A.Y.; Gerasimov, E.Y.; Gromov, N.V.; Medvedeva, T.B.; Saraev, A.A.; Kaichev, V.V. Comparative Study of Photoreforming of Glycerol on Pt/TiO<sub>2</sub> and CuO<sub>x</sub>/TiO<sub>2</sub> Photocatalysts under UV Light. *Mater. Lett.* **2021**, *283*, 128901. [[CrossRef](#)]
48. Le Bail, A. Whole Powder Pattern Decomposition Methods and Applications: A Retrospection. *Powder Diffr.* **2005**, *20*, 316–326. [[CrossRef](#)]
49. Momma, K.; Izumi, F. VESTA 3 for Three-Dimensional Visualization of Crystal, Volumetric and Morphology Data. *J. Appl. Crystallogr.* **2011**, *44*, 1272–1276. [[CrossRef](#)]
50. Kurenkova, A.Y.; Kremneva, A.M.; Saraev, A.A.; Murzin, V.; Kozlova, E.A.; Kaichev, V.V. Influence of Thermal Activation of Titania on Photoreactivity of Pt/TiO<sub>2</sub> in Hydrogen Production. *Catal. Lett.* **2021**, *151*, 748–754. [[CrossRef](#)]